DeepOWT: A global offshore wind turbine data set derived with deep learning from Sentinel-1 data

Thorsten Hoeser[1], Stefanie Feuerstein[1], and Claudia Kuenzer[1,2]

[1]German Remote Sensing Data Center (DFD), German Aerospace Center (DLR), 82234, Wessling, Germany
[2]Department of Remote Sensing, Institute of Geography and Geology, University of Wuerzburg, 97074, Wuerzburg, Germany
Correspondence: Thorsten Hoeser (thorsten.hoeser@dlr.de)

Abstract. Offshore wind energy is at the advent of a massive global expansion. To investigate the development of the offshore wind energy sector, optimal offshore wind farm locations, or the impact of offshore wind farm projects, a freely accessible spatiotemporal data set of offshore wind energy infrastructure is necessary. With free and direct access to such data, it is more likely that all stakeholders who operate in marine and coastal environments are getting involved in the upcoming massive
5 expansion of offshore wind farms. To that end, we introduce the DeepOWT data set (Deep learning derived Offshore Wind Turbines; available at: https://doi.org/10.5281/zenodo.5933967 (Hoeser and Kuenzer, 2022b)), which provides 9,941 locations of offshore wind energy infrastructures along with their deployment stages on a global scale. DeepOWT is based on freely accessible Earth observation data from the Sentinel-1 radar mission. The offshore wind energy infrastructure locations were derived by applying deep learning based object detection with two cascading CNNs (Convolutional Neural Networks) to search
10 the entire Sentinel-1 archive on a global scale. The two successive CNNs have previously been optimised solely on synthetic training examples to detect the offshore wind energy infrastructures in real-world imagery. With a subsequent temporal analysis of the radar signal at the detected locations, the DeepOWT data set reports the deployment stages of each infrastructure in a quarterly frequency from July 2016 until June 2021. The spatiotemporal information is compiled in a ready-to-use GIS (Geo Information System) format to make the usability of the dataset as accessible as possible.

15 ## 1 Introduction

Lately, the expansion of carbon-neutral energy is being strongly promoted (COP26, 2021) (United Nations Framework Convention on Climate Change, Conference Of the Parties). Offshore wind energy is an efficient and reliable energy source and appears to be an important cornerstone for a renewable energy mix (Esteban et al., 2011). For example, the EU (European Union) plans to increase the installed offshore wind energy capacity from 12 GW in 2020 to 300 GW in 2050 toward carbon-
20 neutral energy production. Most of this expansion is planned to be realised in the North Sea Basin (NSB), an already established hot spot for offshore wind energy production. Nevertheless, new sites in the Mediterranean Sea will be developed to achieve the stated goals (EC, 2020). The plans of the European Union are exemplary for a global trend of expanding offshore wind energy projects. Offshore wind farms (OWF) will be deployed to already established offshore wind energy production sites like the East China Sea (ECS). At the same time, the development of new sites for large OWFs, for example, in the Atlantic Ocean

Table 1. Acronyms and abbreviations

AP	Average Precision	GRD	Ground Range Detected
API	Application Programming Interface	GT	Ground Truth
CFAR	Constant False Alarm Rate	IW	Interferometric Wide
CNN	Convolutional Neural Network	NSB	North Sea Basin
COP26	United Nations Framework Convention on Climate Change, Conference Of the Parties	OSM	Open Street Map
DeepOWT	Deep learning derived Offshore Wind Turbine dataset	OWF	Offshore Wind Farm
DoG	Difference of Gaussians	OWT	Offshore Wind Turbine
EC	European Commission	Pr	Precision
ECS	East China Sea	PR	Precision-Recall
ESA	European Space Agency	Rc	Recall
EU	European Union	ResNet-50	ResidualNetwork with 50 convolutional layers
F1	harmonic mean of Precision and Recall	RGB	Red-Green-Blue
Faster R-CNN	Faster Region based Convolutional Neural Network	RPN	Region Proposal Network
FO	False Omission	SAR	Synthetic Aperture Radar
FP	False Positive	SyntEO	Synthetic data generation for Earth Observation
GEE	Google Earth Engine	TP	True Positive
GIS	Geo Information System	UTM	Universal Transverse Mercator
GOWT	Global Offshore Wind Turbine data set by Zhang et al. (2021)	VH	Vertical sent Horizontal received
GPU	Graphics Processing Unit	WGS	World Geodetic System

25 on the East coast of the United States, is ongoing (Rodrigues et al., 2015). Today, the offshore wind energy sector is starting a phase of massive expansion worldwide, affecting marine ecosystems (Drewitt and Langston, 2006; Wilson and Elliott, 2009; Bailey et al., 2014; Bergström et al., 2014; Slavik et al., 2019) as well as stakeholders of different socio-economic sectors active or interested in the same areas, like the fishing industry, shipping routes, military exclusion zones, cultural heritage, residents of coastal areas or the recreational industry (Henderson et al., 2003; Wever et al., 2015; Gusatu et al., 2020; Gușatu et al.,

30 2021; Virtanen et al., 2022). In order to foster the development of offshore wind energy and to provide all stakeholders with free access to data in order to ensure the most sustainable development possible, we introduce the DeepOWT data set, which reports offshore wind turbine (OWT) locations along with their deployment time series for five years from 2016 until 2021 on a global scale.

The proposed DeepOWT data set has been derived from the Sentinel-1 radar archive by applying deep learning based object detection. The employed object detection models were completely trained on synthetic training examples generated by the novel SyntEO (Synthetic data generation in Earth Observation) approach (Hoeser and Kuenzer, 2022a). Thus, the methodological workflow enables the extraction of highly detailed information from extensive Earth observation archives. That way, in addition to the offshore wind energy infrastructure locations, the temporal deployment process can be described at each detected location. This is of major interest for investigating the impact and optimisation measures during the deployment processes, which is an eventful and critical period in an OWT lifecycle. Besides OWT locations, DeepOWT also provides locations of OWF substations and offshore wind energy infrastructures under construction to increase further the information depth and precision of a global OWT data set. Besides this novel information, DeepOWT is openly accessible, comes with valuable ground truth data sets for spatial and temporal evaluation and can easily be used in GIS (Geo Information System) software due to its lightweight size of 4.1 MB and the established .geojson format.

2 Related research

2.1 Deep learning based image analysis in Earth observation

Krizhevsky et al. (2012) proposed the CNN (Convolutional Neural Network) AlexNet during the ImageNet Large Scale Visual Recognition Challenge, which won the contest in 2012. The successful implementation of a deep learning model with many adjustable parameters by using an excessive amount of training data in combination with modern hardware like GPUs (Graphics Processing Units) to optimise the model brought new attention to deep learning and neural networks from many research domains (Krizhevsky et al., 2017; LeCun et al., 2015). CNNs turned out to be particularly suitable for image analysis, e.g. for tasks such as image recognition, image segmentation and object detection. These capabilities make CNNs the most widely used deep learning models in remote sensing (Zhu et al., 2017; Ma et al., 2019; Hoeser and Kuenzer, 2020).

In addition to optical and multispectral Earth observation data, deep learning models have also been increasingly used to analyse radar data from spaceborne Earth observation missions (Zhu et al., 2021). Baumhoer et al. (2019) and Dirscherl et al. (2021) demonstrated how U-Net based CNNs can be used to extract the antarctic coastline and supraglacial lakes from Sentinel-1 data, respectively. Other examples for pixel-wise classifications or image segmentation tasks which exploit Sentinel-1 data with CNNs are the mapping of burned areas (Belenguer-Plomer et al., 2021), crop type mapping (Cué La Rosa et al., 2018; Mullissa et al., 2018) or the classification of irrigated agricultural land (Bazzi et al., 2020). Closely related to the topic of persistent marine infrastructure in this manuscript is the application of ship detection with CNNs and Sentinel-1 data. A considerable number of studies have looked at the extraction of vessels from Sentinel-1 data by employing CNN based object detection models, see Hoeser et al. (2020) for a comprehensive overview.

Multiple studies demonstrate that CNNs can learn the spatial representation of target classes in Sentinel-1 images where they can also take into account spatial context to reduce false positives (Dirscherl et al., 2021; Kang et al., 2017; Hoeser and Kuenzer, 2022a). This property of CNNs is a particularly important argument for using them when extracting object classes from extensive, unfiltered satellite data archives, as demonstrated in this study.

2.2 Offshore wind turbine detection in Earth observation imagery

The detection of persistent offshore infrastructure in Earth observation data has been investigated by applying different approaches. A commonly used approach is the Constant False Alarm Rate (CFAR) as used by Zhang et al. (2019) for marine infrastructure detection. Wong et al. (2019) combined the CFAR approach with a Difference of Gaussians (DoG) preprocessing of the remote sensing radar imagery to increase further the contrast of persistent marine infrastructure and the surrounding sea. Xu et al. (2020) applied order statistic filtering in combination with a derived set of thresholds to extract marine infrastructure from the Landsat and Sentinel-2 missions. Zhang et al. (2021) developed a handcrafted morphologic approach with manual thresholds to identify single OWTs in Sentinel-1 data. All studies have in common that they strongly depend on the high contrast between offshore infrastructure and the surrounding open sea. In a preceding study to this data set, Hoeser and Kuenzer (2022a) proposed an adaptive, deep learning based object detection approach that takes multiscale spatial patterns of the target objects into account to distinguish further different types of offshore infrastructure in a single model.

In 2022, there are three datasets that describe OWT on a global scale, some of which are freely accessible. These are the 4C offshore wind data set (4C Offshore, 2021), OWT locations in the Open Street Map (OSM) project and the Global Offshore Wind Turbine (GOWT v1.3) data set by Zhang et al. (2021). The 4C offshore wind data set collects information about offshore wind projects provided by OWF operators, project descriptions and contracts. It provides an overview of OWF boundaries, single OWT locations and specifications, OWF substations and export cables (4C Offshore, 2021). However, the private company 4C Offshore maintains the 4C offshore wind data set and sells the information. Hence, the data set is only partly accessible to the public and can not freely be used in planning and research to its full extent.

The first open source variant to mention is the OSM project which provides OWT locations in its spatial database. Since OSM data relies on the activity of its community, the accuracy and completeness for OWT locations vary from region to region. Hence, the data set accuracy is not spatially homogenous. Furthermore, there is only a limited temporal consistency in this data set. An entry made in OSM on a specific date does not necessarily correlate with its first appearance in the real world, especially when the temporal accuracy is narrowed down to weeks or months.

The GOWT v1.3 data set demonstrates the possibility of large-scale OWT detection by investigating Earth observation data. In its published version 1.3 it provides OWT locations from 2014 until 2019. Thereby, OWT location is reported as such when it first appears in a remote sensing image. In GOWT v1.3 there is no difference between OWTs under construction and those completed (Zhang et al., 2021). This class indifference leads to a temporally shifted overestimation of the number of power-generating OWTs since the construction phase is not provided separately. Furthermore, GOWT v1.3 does not separately classify OWF substations and has difficulties differentiating them from OWTs, which results in false positive detections of OWTs within OWFs areas.

From these existing data sets and their limitations, the following characteristics have been derived for a global OWT data set:

– Access to all OWT information like location and construction stage in a single file

– Global extent with homogenous reliability

- Temporal consistency regarding the date given in the data set for a single data point and its real-world appearance

- Differentiation between OWTs which are under construction and OWTs which are completed

- Differentiation between OWTs and OWF substations

- Inclusion of latest OWF projects independent of their size, location and construction type

The motivation of this study is to use a deep learning based object detection approach in order to derive a global offshore wind turbine data set with an information depth that is not yet freely available. To that end, we present the DeepOWT (Deep learning derived Offshore Wind Turbines) data set in this study. The main contributions are:

- the presentation of a deep learning based object detection workflow with two cascading CNNs which detect offshore wind farms in the first and single offshore wind energy infrastructure facilities in the second stage.

- the application of the recently proposed SyntEO framework by (Hoeser and Kuenzer, 2022a) for using synthetic data to train the two supervised deep learning models.

- the introduction of the DeepOWT data set with offshore wind energy infrastructure locations on a global scale and quarterly deployment stages for each location from July 2016 until June 2021.

- the differentiation between offshore wind turbines, offshore wind energy substations and offshore wind energy infrastructures under construction for each detected object in the DeepOWT data set.

- the generation of spatiotemporal ground truth data sets of offshore wind energy infrastructures for the two major wind energy production sites, the North Sea Basin and the East China Sea.

- a comprehensive spatiotemporal evaluation of the automatically derived DeepOWT data set.

- free access to the DeepOWT data set and the ground truth data sets created.

3   Materials and methods

3.1   Materials

ESA's (European Space Agency) Copernicus program provides open access to continuously acquired Earth observation data (Aschbacher, 2017). As part of this program, the spaceborne Sentinel-1 SAR (Synthetic Aperture Radar) mission covers mainland and coastal areas on a global scale with a 10 m pixel spacing. The active C-band radar system with a wavelength of 5.6 cm is independent of cloud coverage and able to acquire images day and night (Torres et al., 2012). These specifications make the radar data of the Sentinel-1 mission an excellent source to monitor coastal environments and investigate OWTs on a global scale. All Sentinel-1 acquisitions with the specification IW (Interferometric Wide), GRD (Ground Range Detected) and
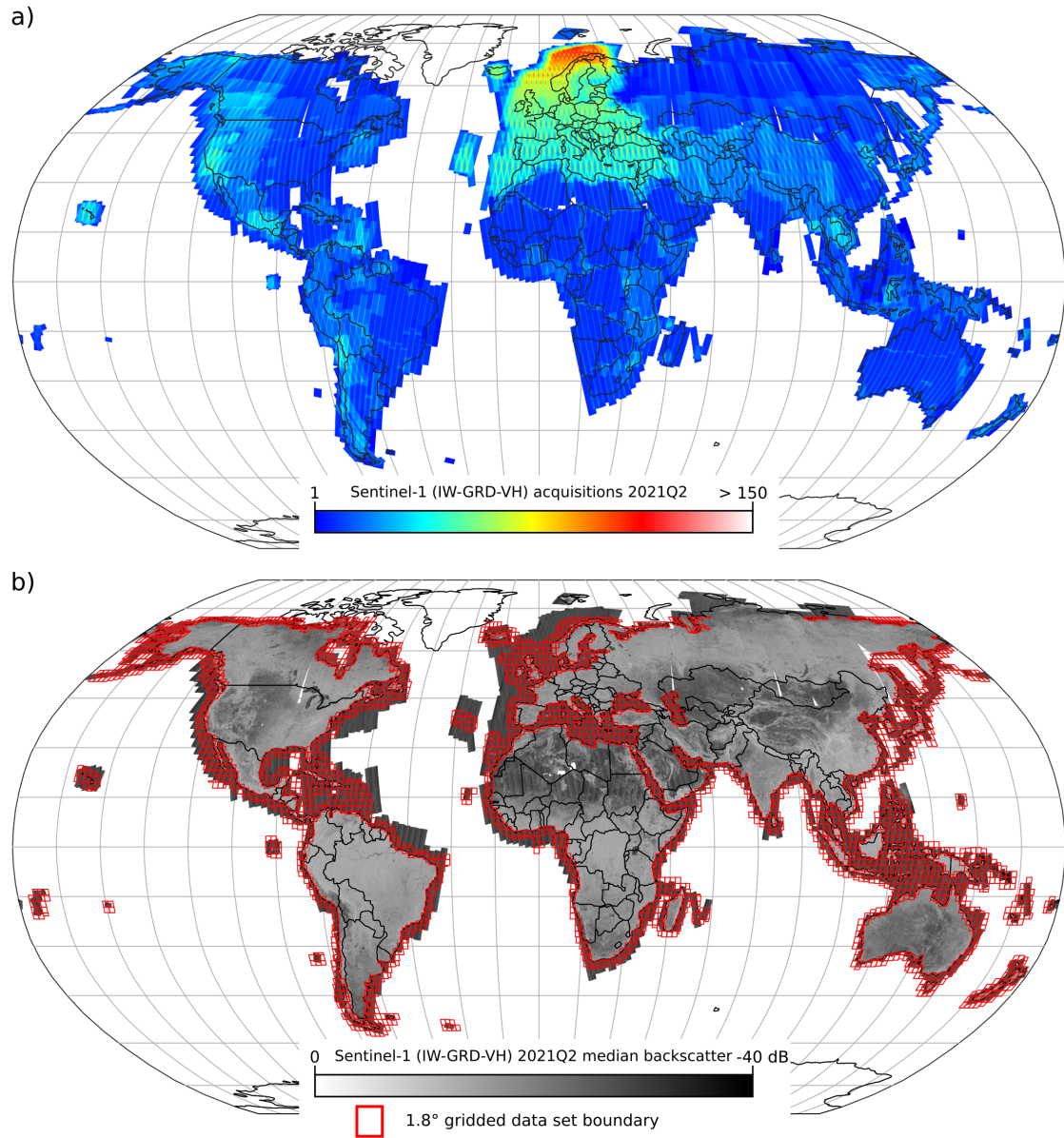
Figure 1. a) Global distribution of the number of all available Sentinel-1 (IW-GRD-VH) acqusitions for the second quater in 2021. b) The corresponding median backscatter amplitude and the data set boundary as 1.8° grid within a buffer of 200 km of the global coastline.

VH (Vertical sent Horizontal received) polarised were chosen as underlying data in this study. Figure 1a) shows how often a location on Earth is sensed by the two Sentinel-1 satellites A and B for the mentioned data product specification in the second quarter of the year 2021. The focus of the Copernicus program becomes visible with a higher number of acquisitions over Europe. Here the satellites acquire data at both ascending and descending orbits, with an inclination of 98.18°. This leads to the X-like pattern and a higher revisit rate compared to other parts of the Earth. In order to harmonise all quarterly acquisitions of the entire Earth to a single global mosaic with a pixel spacing of 10 m, all acquisitions were stacked and reduced to a single band median composite, see figure 1b).

The extent of the study area is defined by a 200 km buffer of the OSM coastline towards the open sea. In order to systematically manage and process the data, a 1.8° regular grid was generated for the entire Earth. All grid cells which intersect the 200 km buffer were selected. The final grid, pictured in figure 1b, defines the area where the DeepOWT data set was detected.

A global Sentinel-1 median composite was queried for the second quarter of 2021 (2021-Q2). Upon this median composite, the global OWF and OWT locations were derived. The Google Earth Engine (GEE) (Gorelick et al., 2017) python API (Application Programming Interface) was used to query the Sentinel-1 data within each 1.8° grid cell. The Sentinel-1 image collection in GEE provides the IW GRD VH acquisitions with additional preprocessing for accurate orbit information, border and thermal noise removal, radiometric calibration and terrain correction. The queried acquisitions within the three-month period were reduced to a median composite with a pixel size of 10 m × 10 m and downloaded. To reduce the amount of data before downloading, the 16 bit floating-point number with a range of 0 to -40, which describes the Sentinel-1 backscatter signal in decibel, were rescaled to 0 to 255 and downloaded as 8 bit integers.

Quarterly subsets from 2016-Q3 to 2021-Q1 were generated the same way as the 2021-Q2 global median composite to investigate temporal deployment dynamics. For these 19 quarterly subsets, the Sentinel-1 median composites were only created if a grid cell contained detected OWTs in 2021-Q2. Thus, the underlying data for the DeepOWT data set are 20 quarterly sets from 2016-Q3 to 2021-Q2. The latest period in 2021-Q2 holds a Sentinel-1 median composite of the entire global coastline. All other 19 sets only store Sentinel-1 median composites for OWF areas present in 2021-Q2.

3.2 Methodology

Figure 2 shows an overview of the methodological workflow to derive the OWT locations and their temporal deployment dynamics of the proposed data set. The core of the workflow is a cascade of two CNN object detectors, where the first CNN detects the OWF boundaries and the second CNN detects OWT locations on the 2021-Q2 global median composite. In order to train both object detector CNNs, two synthetic training data sets were generated in a preceding step. This is the first application of the recently introduced SyntEO approach (Hoeser and Kuenzer, 2022a) embedded in a complete workflow to generate a global data set. After the OWT locations have been detected in the 2021-Q2 data, a time series of 19 quarterly periods is investigated to derive deployment dynamics for each OWT location from 2016-Q3 until 2021-Q1. In a final step, the OWT locations are refined from a bounding box to accurate point locations and combined with the derived deployment time series. Together the spatiotemporal information is saved as a single file which is the DeepOWT data set.
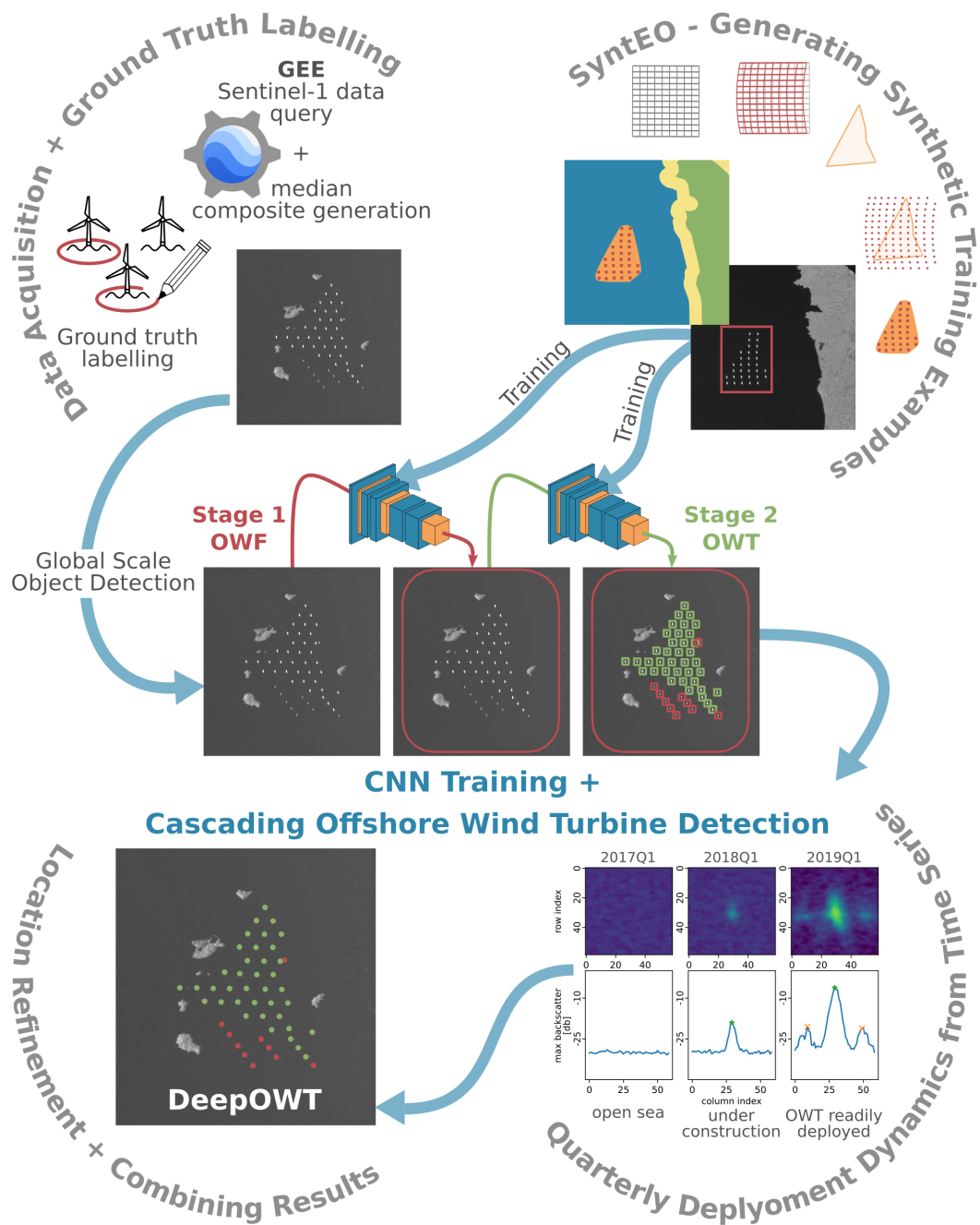
Figure 2. Methodological workflow to generate the DeepOWT data set based on the Sentinel-1 archive. Two CNNs detect OWF and OWT locations, trained on synthetic examples. These spatial detections are used to define their temporal dynamics and accurate location. Finally, DeepOWT combines these spatiotemporal results.

3.2.1 Synthetic training data set generation with SyntEO

In deep learning, layers of untrained weights are stacked to build deep neural networks. In order to adjust the weights in a neural network to succeed in a given task, a large data set with annotated examples is necessary for supervised training (LeCun et al., 2015). The annotation of such large training data sets by hand is time-consuming and, in the case of only a few real-world examples, which applies for OWFs, even impossible. In order to solve these problems, the SyntEO approach was introduced to automatically synthesise large annotated training data sets with a special focus on the needs of Earth observation data. In SyntEO, a domain expert formulates an ontology that describes entities in a remote sensing scene and their spatiotemporal interrelations. The SyntEO ontology is a complex description of nested entities that are related by using topological rules to describe their spatial dependencies. A synthetic image is generated upon the formulated ontology by composing spatially meaningful geometries of all entities to create an abstract scene composition. Hereinafter, sensor-specific texture is added to the geometries of the abstract scene composition to generate the final remote sensing image. Furthermore, annotations are derived from the discrete geometries of the scene composition simultaneously. That way, large deep learning ready data sets can be created fast and automatically. Figure 3 shows a visual summary of the SyntEO process for better intuition. For an in-depth explanation of the SyntEO framework and the underlying ontology concept for automatic data generation in Earth observation, we refer to Hoeser and Kuenzer (2022a).
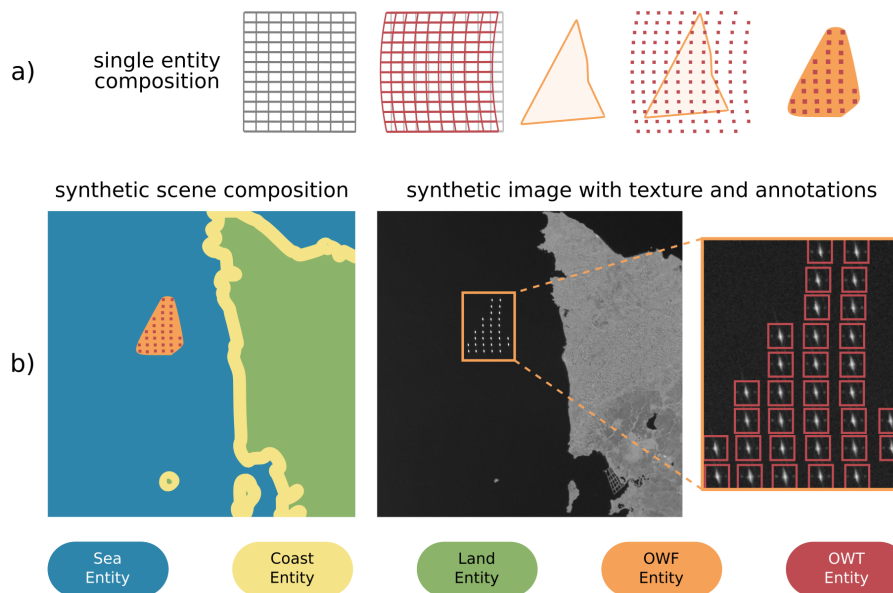
Figure 3. Simplyfied overview of a SyntEO workflow for automatic training example generation (Hoeser and Kuenzer, 2022a). a) visualises how the structure of a single OWF entity is generated. b) shows how multiple entities are composed to a scene composition. The final image is generated by adding texture to the composed scene. The bounding box annotations are derived from the scene composition.

For this study, the ontology drafted by Hoeser and Kuenzer (2022a) was extended to simultaneously generate training examples for OWF and OWT detection. In addition to the origin ontology, which only describes polygon-shaped OWFs, linear-shaped OWFs were introduced to increase the target object variance of the training examples. To further enrich the training data set, non-target classes like synthetically generated oil rigs and images which show the mainland were added with explicitly no annotations to provide negative training examples.

Furthermore, the ontology which has been formulated to generate training examples for OWF detection was reused for OWT detection. Most importantly, the size of the generated images and the annotation were changed. Instead of large-scale bounding box annotations for OWFs in synthetic images with a dimension of 2048×2048 pixel, small-scale bounding box annotations for each OWT were derived from synthetic images with a dimension of 512×512 pixel, see figure 3b). Thus, the CNN object detector, which detects OWTs and other offshore wind energy infrastructures, learns explicitly to focus on small-scale spatial features.

In order to include other targets besides readily deployed OWTs, the non-target class oil rigs in OWF detection was reused. In the second synthetic data set, they are employed to provide annotated examples for OWF substations and offshore wind energy infrastructure under construction. The mainland examples without annotation were kept to provide false positive training examples for OWT detection.

Two pools of training-annotation pairs with additional metadata were generated to compile two balanced synthetic training data sets - one training data set for OWF and the other for single offshore wind energy infrastructure detection. To enable the TensorFlow deep learning framework (Abadi et al., 2016), the selected image annotation pairs were parsed to the TFrecord binary format. That way, the first training data set with 90,000 examples for OWF detection and the second training data set with 275,000 examples for OWT detection were created.

3.2.2 Global OWT object detection with CNNs

Deep learning became an important driver for new insights and methodological developments in Earth system science (Zhu et al., 2017; Reichstein et al., 2019). Recent developments of CNNs allow for the detection of objects in large images by taking spatial context into account (Hoeser and Kuenzer, 2020). For object detection, the two-stage Region based CNN (R-CNN) models are the most commonly used architecture in Earth observation applications (Hoeser et al., 2020). To derive the DeepOWT data set, we used a cascade of two ResNet-50 (ResidualNetwork with 50 convolutional layers) (He et al., 2016) Faster R-CNN (Ren et al., 2015) models, where the first stage of the cascade detects OWF areas on a global scale, and the second stage detects single offshore wind energy infrastructure facilities within the previously detected OWF areas.

The first CNN for OWF detection ingests images with a dimension of 1024×1024 pixel. That requires an on-the-fly downscaling of the training examples for OWF detection, which have a dimension of 2048×2048 pixel. For OWT detection in the second stage of the cascade, the training examples already have a dimension of 512×512 that matches the CNN architecture. Another difference in the model architectures for OWF and OWT detection is the adapted scale factors for the Region Proposal Network (RPN), a submodule of the Faster R-CNN object detector (Ren et al., 2015). In order to adjust the sensitivity for

specific sizes of the target objects, the scale ratios were set to [0.25, 0.5, 1, 2, 3.5] for OWF and [0.25, 0.5] for OWT detection. The scale factors were calculated by applying the approach introduced by Hoeser and Kuenzer (2022a).

The training of the two CNNs was conducted on four parallel NVIDIA RTX 2080Ti GPUs. The training schemes are the same for both architectures. A 0.95-0.05 training-validation split was prepared for both synthetic data sets. A single epoch without any data augmentation was used, which was possible due to the large size and variability of the synthetic data sets. The learning rate was scheduled to decrease smoothly by implementing the cosine decay method (Loshchilov and Hutter, 2017). After a warm-up phase, the base learning rate of 0.01 is reached and then reduced to 0 for all remaining training steps.

The two trained models were used in a cascading manner. The first stage detects OWF by applying a threshold of 0.5 on the prediction score. Thus, the first stage allows a higher false positive rate to include more OWF areas as necessary but avoids false omissions of OWF areas. The second stage detects single offshore wind energy infrastructure facilities within the potential OWF areas by applying a threshold of 0.75 to consider a valid prediction. With the second stage's results, the predictions of the first stage are refined. Potential OWF areas with a share of 90% or more non-OWTs are belatedly dropped as false detection of stage one. This self-checking property of the cascade leads to a high detection rate with a low number of false omissions by simultaneously decreasing false detections. This property was highly suitable for scanning extensive Earth observation archives to find sparsely scattered target objects in large amounts of image data.

Since all predictions are performed on overlapping input tiles, the same object can be detected multiple times. To summarise all predicted bounding boxes in one file, the pixel coordinates of the bounding boxes are translated to the geographic coordinate system WGS84. Furthermore, the bounding boxes were sorted in descending order by their prediction score and indexed with $b = 1, 2, 3...B$, to consolidate the bounding boxes which belong to the same object $\mathcal{B}$. This sorted list of bounding boxes $\mathcal{B}_b$ was unified in a cascading manner if the next box of the list is completely within the unified box or together they have an intersection over union larger than $\tau_{\text{IoU}} = 0.333$, see equation (1).

In order to calculate the exact area of each $\mathcal{B}_b$, the bounding box polygons were temporarily reprojected to their corresponding UTM (Universal Transverse Mercator) coordinate system depending on their UTM zone. The final unified polygons describe the OWF and OWT locations. Figure 4 and 5 show the detection results of the CNN cascade for North Europe and South-East China respectively.

$$
\mathcal{B}_1 := \sum_{b=1}^{B-1} \begin{cases} \mathcal{B}_1 \cup \mathcal{B}_{b+1}, & \text{if} \quad \mathcal{B}_{b+1} \subseteq \mathcal{B}_1 \\ \mathcal{B}_1 \cup \mathcal{B}_{b+1}, & \text{if} \quad \frac{\mathcal{B}_1 \cap \mathcal{B}_{b+1}}{\mathcal{B}_1 \cup \mathcal{B}_{b+1}} > \tau_{\text{IoU}} \\ \mathcal{B}_1, & \text{otherwise} \end{cases}
\tag{1}
$$
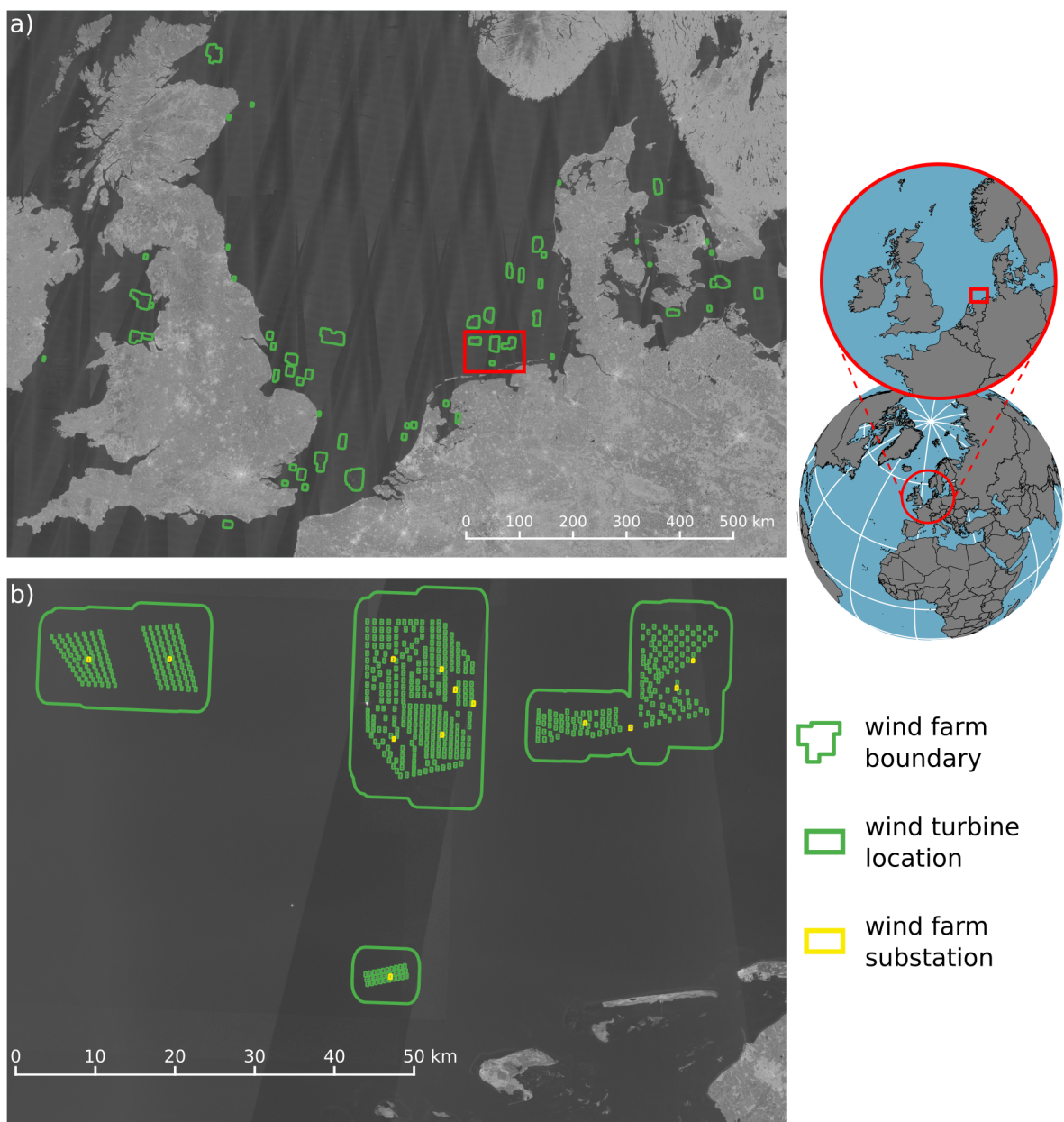
Figure 4. Detection results of the CNN cascade for the North Sea Basin. a) shows the OWFs detected by stage 1, b) the OWT and OWF substations detected by stage 2 within the OWF boundaries of stage 1 in the German Bight.
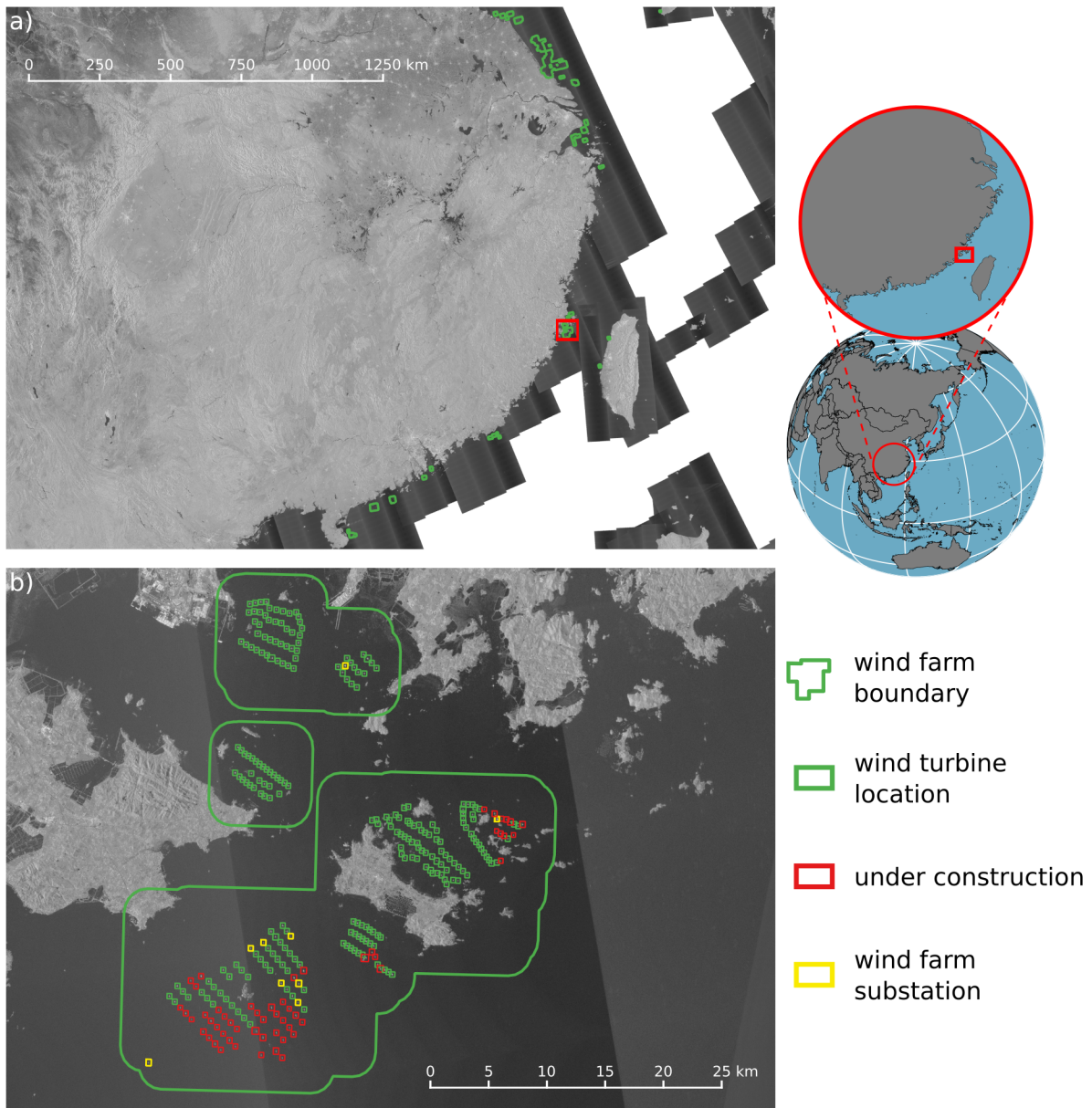
Figure 5. Detection results of the CNN cascade for the South and East China Sea. a) shows the OWFs detected by stage 1, b) the OWT, OWF substations and such under construction detected by stage 2 within the OWF boundaries of stage 1 in the Taiwan Strait.

3.2.3 Time series analysis for deployment dynamics and location refinement

To describe the temporal dynamics of offshore wind energy infrastructure deployment, a backwards-looking time series analysis of the detected locations in 2021-Q2 was performed. For each bounding box of an object location, a multi-temporal
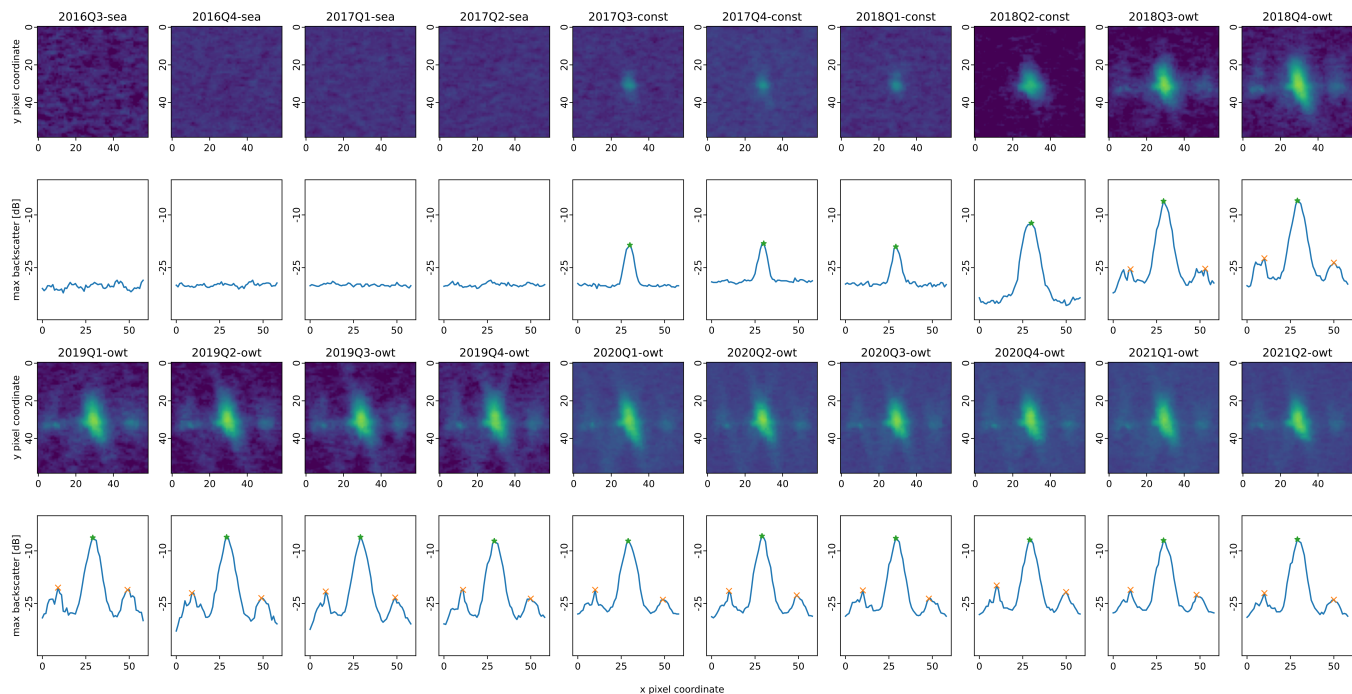
Figure 6. Deployment time series from 2016Q3 until 20201Q2 of an OWT. First and third row show quarterly Sentinel-1 median composites of the same detected bounding box over time. Second and fourth row show the corresponding maximal swath profiles with detected peaks. The automatically derived construction stages are given for each image: sea = open sea/no turbine, const = under construction, owt = offshore wind turbine.

stack of 19 quarterly Sentinel-1 median composites was analysed to determine if an image shows the open sea, an OWT or OWF substation under construction, or an OWT or OWF substation readily deployed. Swath profiles that describe each
240 column's maximum value along the horizontal axes from each image in the multitemporal stack were generated. Figure 6 shows quarterly images and corresponding swath profiles for an OWT deployment time series. By applying two consecutive peak finder algorithms with a high and low prominence (Virtanen et al., 2020) to the swath profile, the centre peak and adjacent peaks to the left and right of the centre peak were detected. In a subsequent analysis which starts in 2021-Q2 with the predicted class of the second stage CNN, the changes in the number of peaks, centre peak amplitude and peak width are investigated to
245 differentiate the deployment stages until 2016-Q3.

To finally refine the bounding boxes of offshore wind energy infrastructure locations to point locations, all pixel values within each bounding box of the 2021-Q2 period were analysed. As with the time series analysis, a maximum swath profile was created along the x-axis, and the centre peak was searched for. With the derived x coordinate and amplitude of the centre peak, the column at the x location of the image patch within the bounding box was queried to find the corresponding
250 y coordinate. By taking the geographic origin of the image patch into account, the WGS84 (World Geodetic System 1984) coordinate for this pixel was derived. Thus, the detected offshore wind energy infrastructure location is no longer described by

a bounding box but by an accurate point location that is precisely at the centre amplitude maximum of the detected object. The final content for the derived data set is completed by merging spatial and temporal processing results.

3.2.4 Data set evaluation

255 In order to evaluate the DeepOWT data set, two ground truth data sets were generated. The test areas are the North Sea Basin (NSB) and the East China Sea (ECS), pictured in figure 7. Their boundaries were aligned with the processing grid of this study. The two areas were chosen due to their importance for offshore wind energy generation, their differences concerning the underlying Sentinel-1 data and the different interaction of OWFs with coastlines, coastal infrastructure and islands. Where the majority of OWFs in the NSB are located within a considerable distance to the coast, in the ECS, OWFs are built closely

260 to small islands and other infrastructures like bridges and harbours, see figure 5. Furthermore, the NSB has a higher number of quarterly Sentinel-1 acquisitions at both orbit directions, whereas the ECS is mainly observed from a single orbit direction and thus has lesser acquisitions at the same time interval, see figure 1. That results in different characteristics of the global Sentinel-1 median composite in both areas. Together, the NSB and ECS represent various OWF types and how they appear in their natural environment and are therefore representational test sites.

265 Two types of ground truth data sets were generated and included as separate files along with the proposed DeepOWT data set. The first type describes the locations of the target objects at a single point in time. The second type describes quarterly time series of deployment dynamics.

Two data sets of the first type were generated, one for 2021-Q2 and one for 2019-Q4. The 2019-Q4 data set will later be used to compare the records of the DeepOWT data set to OSM and GOWT v1.3 records since the latter ends in 2019. For

270 both ground truth data sets, all locations of OWTs and OWF substations, both readily deployed or under construction, were annotated by hand for the entire NSB and ECS. Afterwards, the point locations were buffered with a radius of 100 m, which is the final area that defines a true positive location. To generate the temporal ground truth data sets, about 15% of the 2021-Q2

Table 2. Overview of all ground truth data sets, their corresponding time stamp and number of objects in each class. * are the numbers for the start in 2016Q3 and end in 20201Q1 of the ground truth time series. † is the number of all hand labelled classes of the entire ground truth time sereis with 19 intervals.

Site	Time stamp	Data set name	OWT	Construction	Substation	Open sea	$\sum$ label
NSB	2021Q2	2021Q2_nsb	4,016	253	85	-	4,354
ECS	2021Q2	2021Q2_ecs	2,208	574	62	-	2,844
NSB	2019Q4	2019Q4_nsb	3,571	172	78	-	3,821
ECS	2019Q4	2019Q4_ecs	1,208	214	47	-	1,469
NSB	2016Q3-2021Q1	16Q3-21Q1_nsb	352-583*	59-47*	12-19*	227-1*	12,350[†]
ECS	2016Q3-2021Q1	16Q3-21Q1_ecs	40-311*	12-87*	3-11*	375-21*	8,170[†]
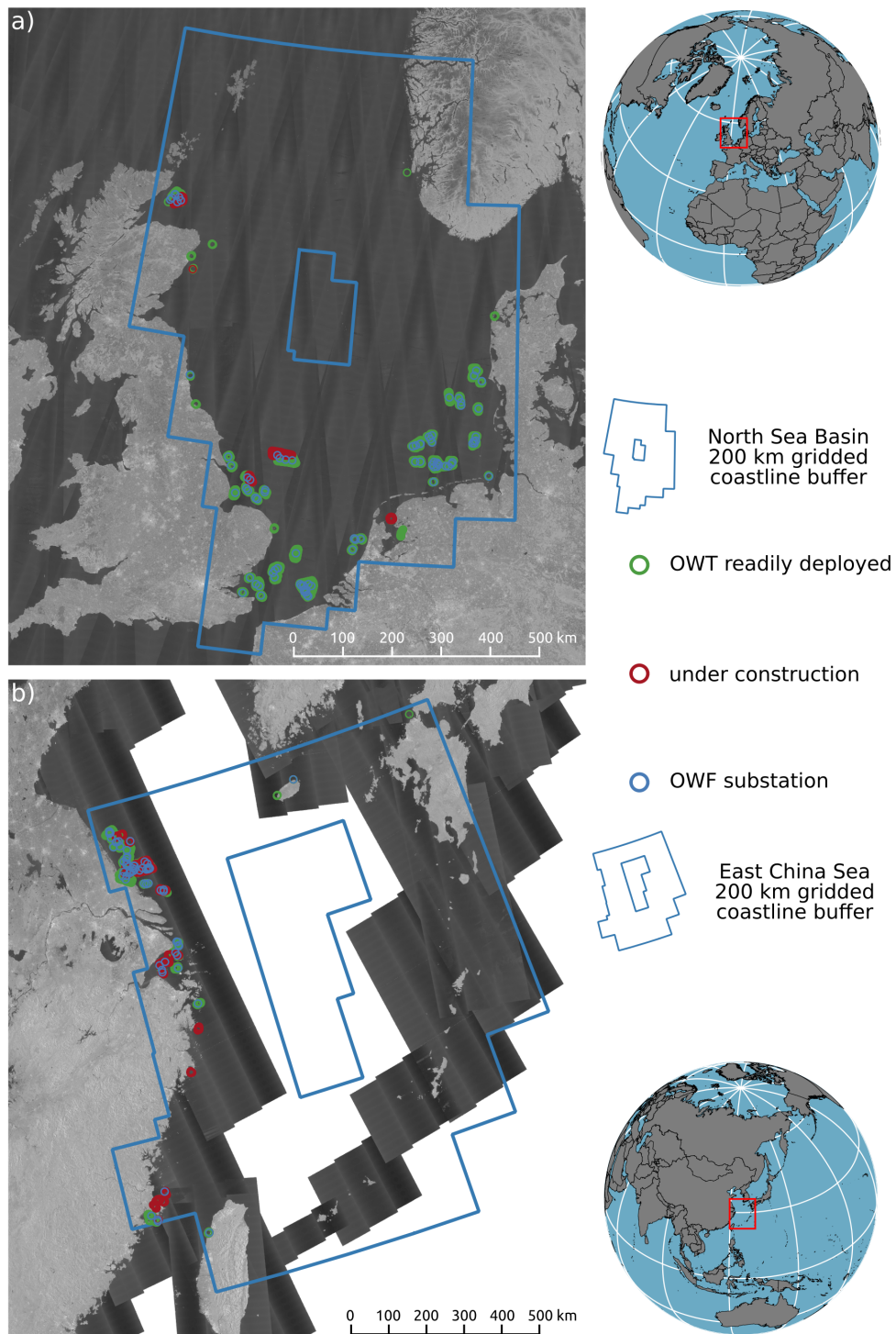
Figure 7. Overview of the ground truth sites boundaries and the hand labelled object locations and deployment stages for the second quarter in 2021. a) shows the North Sea Basin (NSB), b) the East China Sea (ECS).

ground truth locations were selected for both the NSB and the ECS variant. For these selected locations, the entire quarterly time series from 2016-Q3 until 2021-Q2 was annotated by hand. An overview of the different ground truth data sets and their number of annotated target objects is provided in table 2.

During manual ground truth data labelling, all locations and temporal intervals were visually examined and cross-checked with different data sources. Therefore, Sentinel-1 images were investigated in combination with additional RGB (Red-Green-Blue) images from Sentinel-2 and Google Earth. Furthermore, public information concerning the deployment dynamics provided by official planning documents, OWF operators and news portals were conducted mainly to validate the labels of the temporal ground truth data sets.

Following the manual generation of the ground truth data sets, we calculated evaluation metrics to assess the automatically derived DeepOWT data set. To provide consistent and comparable metrics that take the different numbers of objects for each test site into account, the metrics were calculated separately in the first step. A predicted object is considered a true positive (TP) when it is within the ground truth polygon, a 100 m radius around the object centre of a test label, and the predicted point and test polygon have the same class. Otherwise, it is a false positive (FP). A wrongly omitted ground truth polygon is considered a false omission (FO). Upon that, precision Pr and recall Rc were calculated:

$$\mathrm{Pr} = \frac{\mathrm{TP}}{\mathrm{TP} + \mathrm{FP}} \tag{2}$$

$$\mathrm{Rc} = \frac{\mathrm{TP}}{\mathrm{TP} + \mathrm{FO}} \tag{3}$$

The harmonic mean of Pr and Rc, summarises both metrics as the F1 score:

$$\mathrm{F1} = 2 \times \frac{\mathrm{Pr} \times \mathrm{Rc}}{\mathrm{Pr} + \mathrm{Rc}} \tag{4}$$

Furthermore, all detections made by a CNN were sorted by their prediction scores in descending order and indexed with $c = 1, 2, ..., C$. From this ordered list, an all point interpolated precision-recall curve $\mathrm{Pr}_{\mathrm{interp}}$ is generated.

$$\mathrm{Pr}_{\mathrm{interp}} = \max_{\tilde{\mathrm{Rc}}:\ \tilde{\mathrm{Rc}} \geq \mathrm{Rc}} \mathrm{Pr}_{\mathrm{interp}}(\tilde{\mathrm{Rc}}) \tag{5}$$

Finally, the area under the all-point interpolated precision-recall curve describes the average precision AP (Padilla et al., 2021),

$$\mathrm{AP} = \sum_{c=1}^{C} (\mathrm{Rc}(c) - \mathrm{Rc}(c-1)) \times \mathrm{Pr}_{\mathrm{interp}}(\mathrm{Rc}(c)), \tag{6}$$

with $\mathrm{Rc}(0) = 0$.

In order to report overall metrics for all n sites or intervals of a time series, the separately calculated metrics were combined by macro averaging:

$$300 \quad \mathrm{Pr}_{\mathrm{avg}} = \frac{1}{n} \sum_{i=1}^{n} \mathrm{Pr}_i \tag{7}$$

$$\mathrm{Rc}_{\mathrm{avg}} = \frac{1}{n} \sum_{i=1}^{n} \mathrm{Rc}_i \tag{8}$$

$$\mathrm{F1}_{\mathrm{avg}} = \frac{1}{n} \sum_{i=1}^{n} \mathrm{F1}_i \tag{9}$$

Thus the macro $\mathrm{F1}_{\mathrm{avg}}$ score is defined as the arithmetic mean over harmonic means following (Opitz and Burst, 2021).

4 Results

305 The derived DeepOWT data set contains 9,941 offshore wind energy infrastructure locations on a global scale. Each detected location is associated with 20 quarterly deployment stages from July 2016 until June 2021, which inform about the deployment process and the object class to further specify the offshore wind energy infrastructure type. The potential three classes are offshore wind turbines, offshore substations, and offshore wind energy infrastructure under construction. If no infrastrucutre
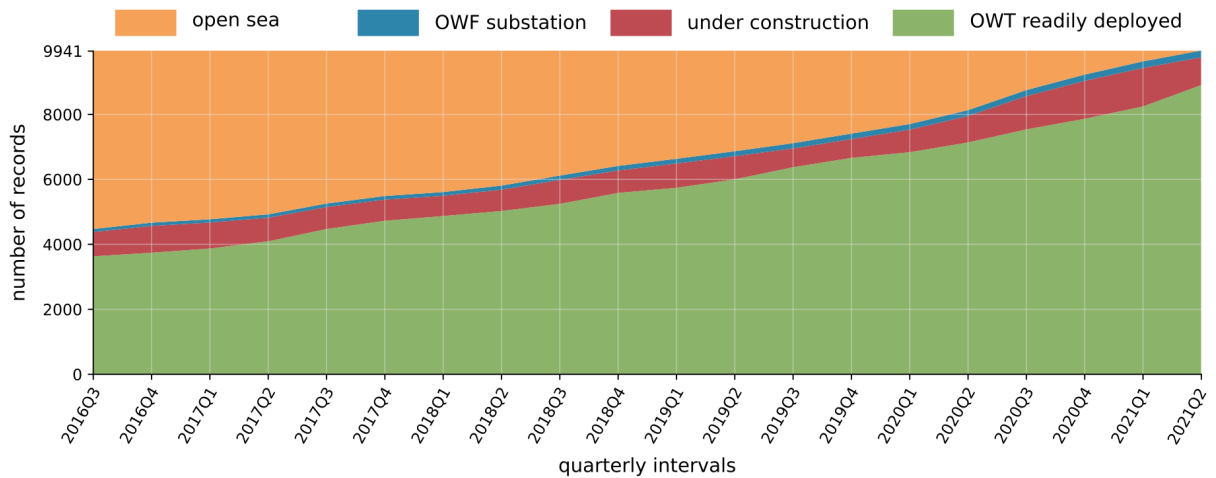
Figure 8. The temporal development of all 9,941 objects and their corresponding class in the DeepOWT data set. Class and location in an interval with an * were derived by a CNN. In all other intervals, the class was derived by the swath profile analysis, see figure 6.

 Figure 8 provides an overview of all detected objects and their

310 corresponding classes over the entire time series in the DeepOWT data set from July 2016 until June 2021.

4.1 Evaluation results

Table 3. Overview of all calculated metrics for the CNN cascade detections on the 2021Q2 global Sentinel-1 median composite for each class separately. The detections were evaluated with the 2021Q2_nsb (North Sea Basin) and 2021Q2_ecs (East China Sea) ground truth data sets.

Site	Class	GT	TP	FP	FO	Pr	Rc	F1	AP
North Sea Basin	OWT	4,016	3,996	1	20	1.0	0.995	0.997	0.995
North Sea Basin	under construction	253	186	7	67	0.964	0.735	0.834	0.72
North Sea Basin	OWF substation	85	74	2	11	0.974	0.871	0.919	0.859
East China Sea	OWT	2,208	2,168	16	40	0.993	0.982	0.987	0.981
East China Sea	under construction	574	393	7	181	0.982	0.685	0.807	0.678
East China Sea	OWF substation	62	56	6	6	0.903	0.903	0.903	0.853
						Pr_{avg}	Rc_{avg}	$F1_{avg}$	
Combined	OWT	6,224	6,164	17	60	0.996	0.988	0.992	
Combined	under construction	827	579	14	248	0.973	0.71	0.821	
Combined	OWF substation	147	130	8	17	0.938	0.887	0.911	
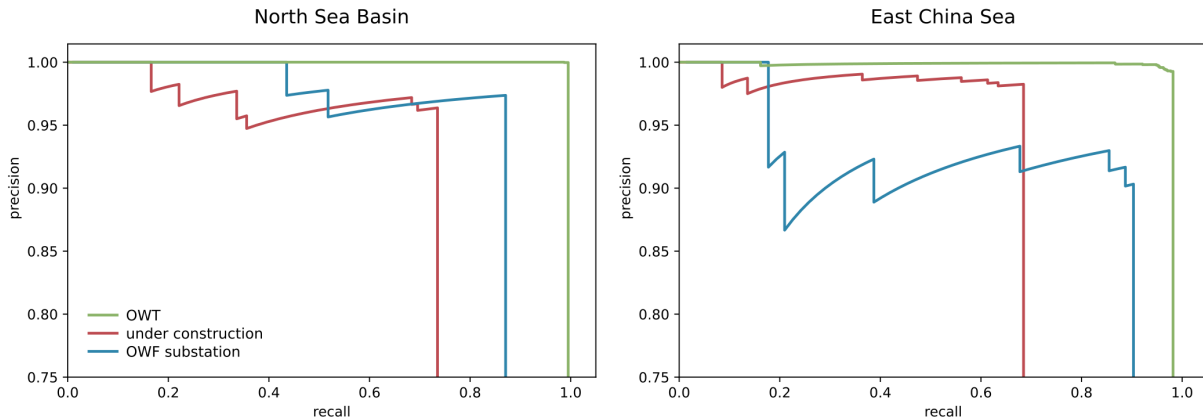
Figure 9. Precision recall curves for the CNN cascade detections on the 2021Q2 global Sentinel-1 median composite for each class separately. The detections were evaluated with the 2021Q2_nsb (North Sea Basin) and 2021Q2_ecs (East China Sea) ground truth data sets. The AP values from table 3 are the corresponding areas under the interpolated precision recall curves.
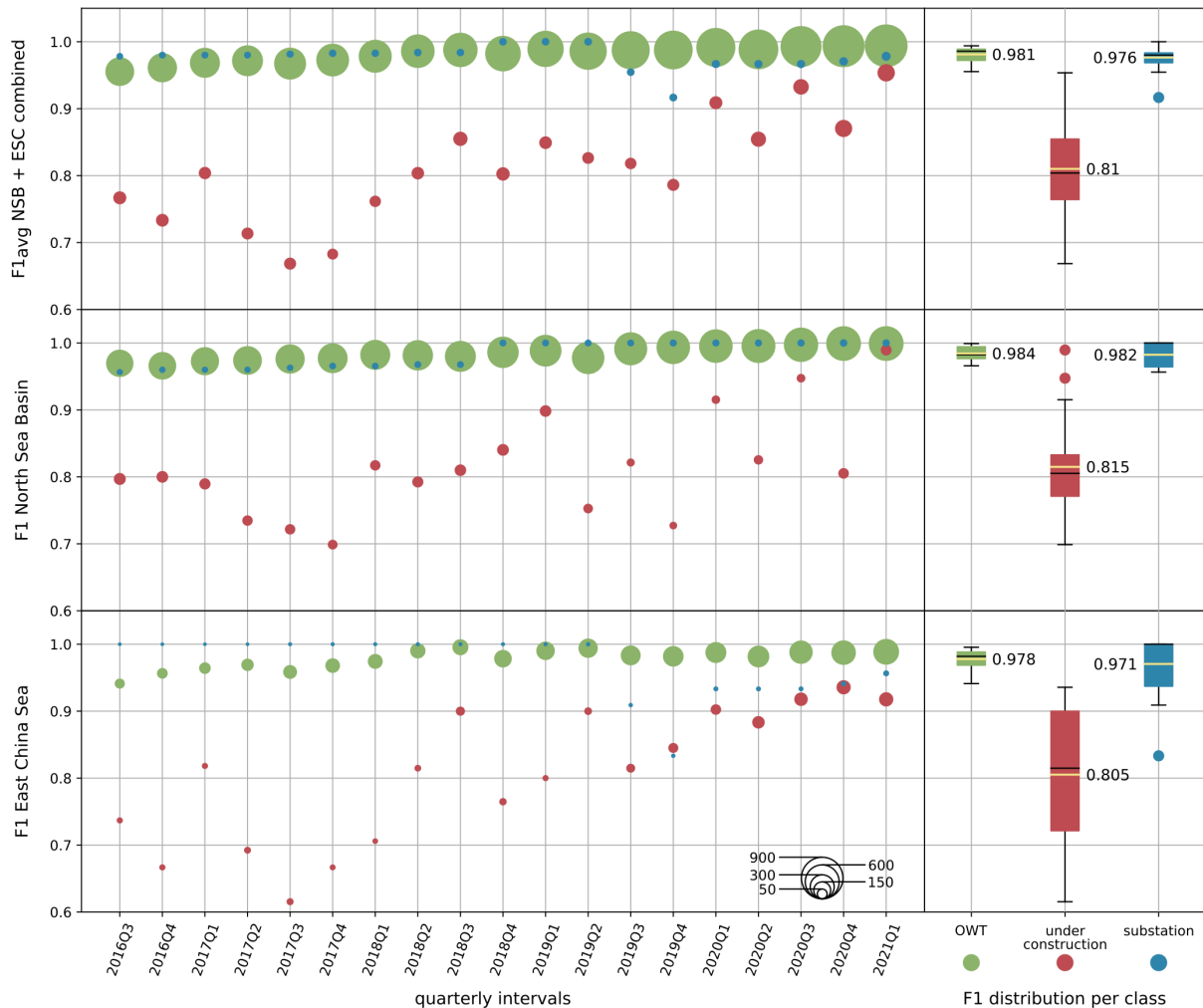
Figure 10. F1 scores for quarterly intervals pictured as points, where the point size describes the number of ground truth labels. On the right side, boxplots describe the F1 time series for each class and provide the temporal $F1_{avg}$ over the entire time series. The data was evaluated on the 16Q3-21Q1_nsb (North Sea Basin) and 16Q3-21Q1_ecs (East China Sea) ground truth data sets.

Table 3 and figure 9 summarise the evaluation results of the objects detected by the CNN cascade in the latest interval (2021-Q2). The evaluation results show that the performance is stable across both study sites. Thus, the CNN models trained on synthetic data can handle both test site characteristics equally well despite the more challenging conditions in the ECS.

315   OWT detection is of the highest quality with a $F1_{avg}$ score of 99.2%. Furthermore, the $F1_{avg}$ score for OWF substations is at 91.1%. Offshore wind energy infrastructure under construction appears to be the most challenging class, which can be explained as follows. An OWT under construction's first real-world appearance can be restrained in median images when their onset is at the end of a quarter, and thus, just a small amount of Sentinel-1 acquisitions contribute to the quarterly median

composite. Also, due to the unspecific spatial pattern of single OWT under construction, they are falsely rejected since they
are similar to small islands and other persistent marine infrastructure. The PR-curve in figure 9 supports this interpretation,
which clearly shows that when an OWT under construction is recognised, it always is a true positive resulting in high precision.
However, the PR-curve drops sharply at a high precision level around a recall level of 0.7. That indicates false omissions, which
can also be seen in table 3. However, the class OWT under construction still has a $F1_{avg}$ score of 82%.

Figure 10 shows the results of the time series evaluation. For each class and interval, the F1 scores were calculated. The
boxplots on the right side show their distribution and the $F1_{avg}$ over the entire time series. The combined assessment reports
the $F1_{avg}$ in each period by averaging the corresponding results from the two ground truth sites. The results show that the time
series analysis performs equally well on both sites, similar to the performance of the CNN cascade. OWT have a $F1_{avg}$ of
98.1%, OWF substations of 97.6% and offshore wind energy infrastructure under construction of 81%.

4.2 Data set comparison

As reported in section 2, two openly accessible data sets exist, which describe OWT locations, these are OWT records in the
OSM database and the GOWT v1.3 data set (Zhang et al., 2021). Since the GOWT v1.3 data set holds records until December
2019, all entries until 2019Q4 of the DeepOWT data set were chosen to perform the comparison. Likewise, for OSM records
of OWTs, only those entries were queried that were registered by 31.12.2019. The evaluation metrics for all three data sets
were calculated on the 2019Q4_nsb and 2019Q4_ecs ground truth data sets.

Since OSM describes locations of readily deployed OWT, only the class 'owt' from DeepOWT was assessed. The com-
parison in figure 11 shows a consistently better performance of DeepOWT compared to entries of the OSM database. It also
becomes clear that the availability of OWT entries in the OSM database differs significantly between the two ground truth
sites. In comparison, the records of the DeepOWT data set, which were derived from remote sensing data, show similar and
consistently better performance metrics on both sites. This clearly shows the advantages of remote sensing data based OWT
detection on a global scale.
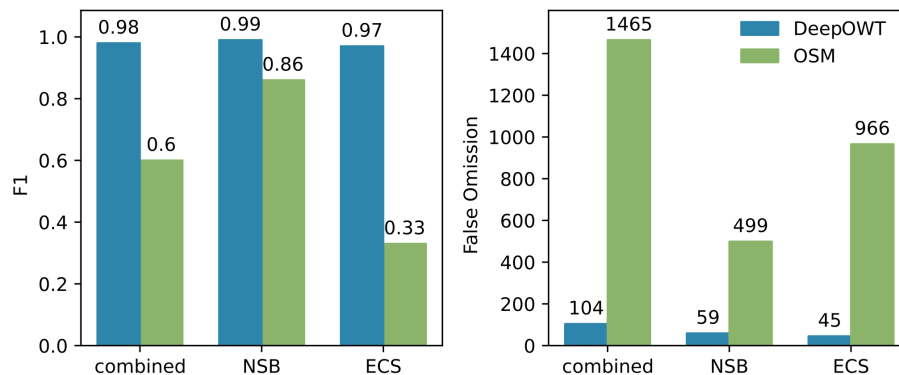
Figure 11. Comparision of the F1 score and false omissions from the OSM and DeepOWT data sets for readily deployed OWT locations in
2019Q4. The data sets were evaluated with the 2019Q4_nsb (North Sea Basin) and 2019Q4_ecs (East China Sea) ground truth data sets.

GOWT v1.3 contains OWT locations, classified as such when the construction of a turbine foundation starts. Yet, it does not distinguish between OWTs under construction and those completed. Therefore, the 'under construction' and 'owt' classes of the DeepOWT data set were combined to compare the results with GOWT v1.3 records. The comparison in figure 12 shows that both remote sensing based data sets perform consistently on both test sites. Nevertheless, this study's deep learning-based DeepOWT data set performs better than GOWT v1.3, which has been derived by applying a handcrafted morphologic approach for OWT detection.
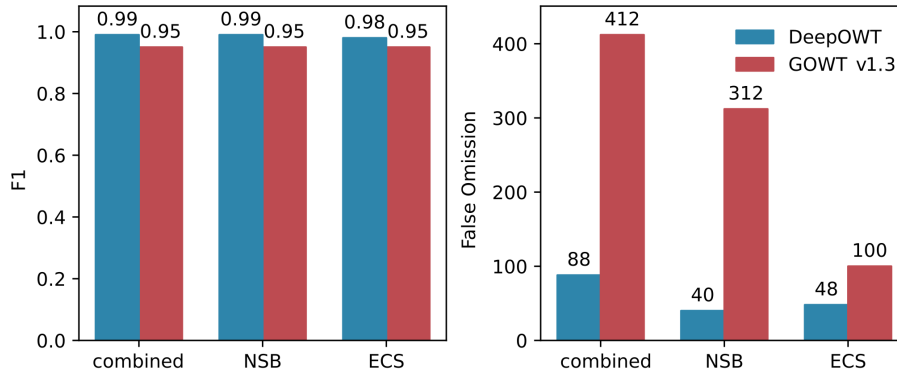
Figure 12. Comparision of the F1 score and false omissions from the GOWT v1.3 and DeepOWT data sets for readily deployed OWT and OWT under construction in 2019Q4. The data sets were evaluated with the 2019Q4_nsb (North Sea Basin) and 2019Q4_ecs (East China Sea) ground truth data sets.

4.3 Technical description

DeepOWT (Deep learning derived Offshore Wind Turbines) is introduced with version number 1.21.2, where the first number is increased when significant changes are made to the methodology used to detect the OWF and OWT objects automatically or additional content is appended to the data set. The second and third numbers describe the year and quarter of the latest interval recorded in the data set. With this, methodological and temporal information is incorporated into the data set name and versioning.

The data set contains the automatically derived target location and the earlier described hand-labelled ground truth data sets. Table 4 provides an overview of which data set file contains which information. DeepOWT 1.21.2 describes the deployment stages of OWT and OWF substations on a global scale from 2016-Q3 until 2021-Q2. Each entry holds the information of the deployment stage within three months of the respective quarter in a year. 9,737 OWTs were detected for the second quarter of 2021. Of these, 8,885 were readily deployed, and 852 were under construction. Additionally, 204 OWF substations were detected for the same period. The file size of DeepOWT is 4.1 MB.

All automatically detected and hand labelled objects are described as points or polygons using the geographic coordinate system WGS84. The spatial geometries were checked topologically to identify duplicate entries, even if no topological errors were found during this inspection. The checked geometries are stored in `.geojson` files along with the temporal deployment

Table 4. Overview of the metadata of all files included in the DeepOWT data set.

File	Extent	Time stamp	Periods	Geometry	OWT	const	sub	sea	Entries
DeepOWT.geojson	global	2016Q3-2021Q2	20	points	✓	✓	✓	✓	9,941
gt_2021Q2_nsb.geojson	NSB	2021Q2	1	polygons	✓	✓	✓	✗	4,354
gt_2021Q2_ecs.geojson	ECS	2021Q2	1	polygons	✓	✓	✓	✗	2,844
gt_2019Q4_nsb.geojson	NSB	2019Q4	1	polygons	✓	✓	✓	✗	3,821
gt_2019Q4_ecs.geojson	ECS	2019Q4	1	polygons	✓	✓	✓	✗	1,469
gt_2016Q3-2021Q1_nsb.geojson	NSB	2016Q3-2021Q1	19	polygons	✓	✓	✓	✓	650
gt_2016Q3-2021Q1_ecs.geojson	ECS	2016Q3-2021Q1	19	polygons	✓	✓	✓	✓	430
gt_nsb_gridded.geojson	NSB	-	-	polygons	✗	✗	✗	✗	1
gt_ecs_gridded.geojson	ECS	-	-	polygons	✗	✗	✗	✗	1

Table 5. Mapping of the key in integer format, used in the data set files, to semantic labels and their abbreviations.

Data set key	Semantic label	Abbreviation
0	open sea	sea
1	under construction	const
2	offshore wind turbine	owt
3	offshore wind farm substation	sub

information as corresponding attribute table. The quarterly periods of the time series in the attribute table of a `.geojson` file are named in the format Y$yyyy$Qq, where $yyyy$ is the year and q the quarter of a year. For each location and time series record, the object class or deployment stage is described as an integer between 0 and 3. Table 5 provides the mapping of the

365 corresponding semantic labels.

4.4 Potential data set applications

Due to the increasing expansion of OWFs at existing and recently newly developed sites for wind energy production, a holistic understanding and detailed insights of the expansion process are gaining importance (Fox et al., 2006; Gușatu et al., 2021; Johnson et al., 2022). The proposed DeepOWT data set enables all stakeholders involved to access OWT deployment time series

370 globally. Thereby, the division in the pre-, meanwhile, and post-construction phases of the deployment process is particularly important. OWT operators can use this information to develop optimisation measures for the necessary construction process with a specific focus on environmental conditions. Furthermore, single turbine locations on a global scale and under different

conditions enable operators to investigate OWFs beyond their own facilities to optimise efficiency during the energy production phase and make better location decisions.

375   Since OWF often expand in areas that are already used as fishing grounds, shipping routes or are, to some extent, restricted areas like nature reserves or military exclusion zones, potential conflicts have to be recognised early and solved by integrated spatial planning towards multi-use concepts of marine space (Wever et al., 2015; Gusatu et al., 2020). DeepOWT supports the investigation and documentation of OWF projects and potential conflicts to apply the insights to upcoming projects at an early planning phase.

380   The ecological impacts of OWFs are manifold and have to be differentiated on a spatiotemporal scale (Drewitt and Langston, 2006; Wilson and Elliott, 2009; Bailey et al., 2014; Bergström et al., 2014; Slavik et al., 2019). Thus the spatially contextualised deployment time series in DeepOWT are an important data source for investigations of how habitats and migration routes of marine wildlife are impacted. For policymakers, DeepOWT offers the opportunity to quickly overview OWF expansion and compare trends on multiple scales in space and time (Rodrigues et al., 2015). Finally, DeepOWT can be used as a database to

385   foster the exchange and transfer of knowledge between different stakeholders, which was found to be of high importance in offshore wind energy projects (Henderson et al., 2003; Fox et al., 2006; Wever et al., 2015; Gusatu et al., 2020).

From a technical perspective, DeepOWT offers a direct integration in analysis made with GIS software and spatial databases (Cavazzi and Dutton, 2016; Gusatu et al., 2020). The lightweight file size and structure of OWT locations, which summarises petabytes of underlying remote sensing images, enables fast processing even on mobile devices. Thus the DeepOWT data set

390   can be used in computational heavy GIS analysis as well as in field campaigns to enrich on-site mapping information.

5   Data availability

The DeepOWT data set is freely available at https://doi.org/10.5281/zenodo.5933967 (Hoeser and Kuenzer, 2022b). Additionally, the Coastal Explorer (https://coastalx.eoc.dlr.de/) made with the UKIS frontend library (Boeck et al., 2022) provides an interactive overview of the derived OWF boundaries and offshore wind energy infrastructure locations along with their

395   temporal deployment dynamics.

6   Conclusions

This study introduced DeepOWT (Deep learning derived Offshore Wind Turbines), the first openly accessible data set that provides offshore wind turbine (OWT) locations along with their quarterly deployment stages on a global scale. DeepOWT is derived from the data provided by the spaceborne C-band radar mission Sentinel-1. All available acquisitions along the global

400   coastline between July 2016 and June 2021 were used to build quarterly median composites. The latest median composite from 2021 was investigated by using deep learning-based object detection. A cascade of two convolutional neural networks subsequently detects potential offshore wind farm (OWF) locations and single OWT and OWF substations within these areas. The two CNNs were trained entirely on synthetic training data generated using the novel SyntEO approach for Synthetic data

generation in Earth Observation (Hoeser and Kuenzer, 2022a). Based on the detections of the CNN cascade, a quarterly time series was derived, which describes the deployment dynamics for every offshore wind energy infrastructure location between 2016 and 2021.

The data set covers 8,885 OWTs, 852 platforms under construction and 204 OWF substations for the latest period, the second quarter of 2021. The majority of OWTs are located in the North Sea Basin and the East and South China Sea. With equally good performance on the two ground truth data sets in the North Sea Basin and East China Sea, the quality of the data set is consistent over time and space. It securely describes large OWFs far off the coast as well as small OWFs in complex near-coast environments. The DeepOWT data set contains nine `.geojson` files, one with the predicted offshore wind energy infrastructure locations and deployment time series, and eight additional files which describe the ground truth data. With a file size of 4.1 MB, DeepOWT is easily portable and ready to use in GIS software.

DeepOWT contributes to a holistic understanding as well as detailed insights into the ongoing development of the offshore wind energy sector, which is at the beginning of a massive expansion phase on a global scale. Furthermore, DeepOWT proves the possibility of automatically detecting small-scale objects within large Earth observation archives of radar acquisitions without using auxiliary data by applying state-of-the-art deep learning methods. With the continuation of the Sentinel-1 mission secured, a future detection of OWT deployment time series on a global scale is possible.

Author contributions. TH designed the study, labelled the ground truth data, developed and implemented the code for data processing, visualisation and evaluation, and prepared the original manuscript, including figures. SF technically implemented the data visualisation in the web mapping service. CK supervised the study, gave suggestions for figures and repeatedly commented and discussed the manuscript. TH and CK revised the manuscript.

Competing interests. The contact author has declared that neither they nor their co-authors have any competing interests.

Acknowledgements. The authors would like to thank ESA's Copernicus program for providing free access to the Sentinel-1 data and the Google Earth Engine platform for preprocessing and making the data accessible. Furthermore, we would like to thank the OpenStreetMap project for providing offshore wind turbine locations and the global coastline data. Finally, we would like to thank the two anonymous reviewers for their time revising our manuscript and valuable comments.

References

4C Offshore: 4C Offshorewind, https://map.4coffshore.com/offshorewind/, 2021.

430 Abadi, M., Barham, P., Chen, J., Chen, Z., Davis, A., Dean, J., Devin, M., Ghemawat, S., Irving, G., Isard, M., Kudlur, M., Levenberg, J., Monga, R., Moore, S., Murray, D. G., Steiner, B., Tucker, P., Vasudevan, V., Warden, P., Wicke, M., Yu, Y., and Zheng, X.: TensorFlow: A System for Large-Scale Machine Learning, in: 12th USENIX Symposium on Operating Systems Design and Implementation (OSDI 16), pp. 265–283, USENIX Association, Savannah, GA, https://www.usenix.org/conference/osdi16/technical-sessions/presentation/abadi, 2016.

435 Aschbacher, J.: ESA's earth observation strategy and Copernicus, in: Satellite earth observations and their impact on society and policy, pp. 81–86, Springer, Singapore, https://doi.org/10.1007/978-981-10-3713-9_5, 2017.

Bailey, H., Brookes, K. L., and Thompson, P. M.: Assessing environmental impacts of offshore wind farms: lessons learned and recommendations for the future, Aquatic Biosystems, 10, https://doi.org/10.1186/2046-9063-10-8, 2014.

Baumhoer, C. A., Dietz, A. J., Kneisel, C., and Kuenzer, C.: Automated Extraction of Antarctic Glacier and Ice Shelf Fronts from Sentinel-1

440 Imagery Using Deep Learning, Remote Sensing, 11, https://doi.org/10.3390/rs11212529, 2019.

Bazzi, H., Ienco, D., Baghdadi, N., Zribi, M., and Demarez, V.: Distilling Before Refine: Spatio-Temporal Transfer Learning for Mapping Irrigated Areas Using Sentinel-1 Time Series, IEEE Geoscience and Remote Sensing Letters, 17, 1909–1913, https://doi.org/10.1109/LGRS.2019.2960625, 2020.

Belenguer-Plomer, M. A., Tanase, M. A., Chuvieco, E., and Bovolo, F.: CNN-based burned area mapping using radar and optical data,

445 Remote Sensing of Environment, 260, 112 468, https://doi.org/10.1016/j.rse.2021.112468, 2021.

Bergström, L., Kautsky, L., Malm, T., Rosenberg, R., Wahlberg, M., Capetillo, N. Å., and Wilhelmsson, D.: Effects of offshore wind farms on marine wildlife—a generalized impact assessment, Environmental Research Letters, 9, 034 012, https://doi.org/10.1088/1748-9326/9/3/034012, 2014.

Boeck, M., Voinov, S., Keim, S., Volkmann, R., Langbein, M., and Mühlbauer, M.: Frontend Libraries for DLR UKIS (Map) Applications.

450 Version v8.0.1, https://doi.org/10.5281/zenodo.5835895, 2022.

Cavazzi, S. and Dutton, A.: An Offshore Wind Energy Geographic Information System (OWE-GIS) for assessment of the UK's offshore wind energy potential, Renewable Energy, 87, 212–228, https://doi.org/10.1016/j.renene.2015.09.021, 2016.

COP26: Global coal to clean power transition statement, https://ukcop26.org/global-coal-to-clean-power-transition-statement/, 2021.

Cué La Rosa, L. E., Happ, P. N., and Feitosa, R. Q.: Dense Fully Convolutional Networks for Crop Recognition from Multitemporal

455 SAR Image Sequences, in: IGARSS 2018 - 2018 IEEE International Geoscience and Remote Sensing Symposium, pp. 7460–7463, https://doi.org/10.1109/IGARSS.2018.8517995, 2018.

Dirscherl, M., Dietz, A. J., Kneisel, C., and Kuenzer, C.: A Novel Method for Automated Supraglacial Lake Mapping in Antarctica Using Sentinel-1 SAR Imagery and Deep Learning, Remote Sensing, 13, https://doi.org/10.3390/rs13020197, 2021.

Drewitt, A. L. and Langston, R. H. W.: Assessing the impacts of wind farms on birds, Ibis, 148, 29–42, https://doi.org/10.1111/j.1474-

460 919X.2006.00516.x, 2006.

EC, E. C.: An EU Strategy to harness the potential of offshore renewable energy for a climate neutral future, https://ec.europa.eu/energy/sites/ener/files/offshore_renewable_energy_strategy.pdf, 2020.

Esteban, M. D., Diez, J. J., López, J. S., and Negro, V.: Why offshore wind energy?, Renewable Energy, 36, 444–450, https://doi.org/10.1016/j.renene.2010.07.009, 2011.

465   Fox, A., Desholm, M., Kahlert, J., Christensen, T. K., and Krag Petersen, I.: Information needs to support environmental impact assessment of the effects of European marine offshore wind farms on birds, Ibis, 148, 129–144, https://doi.org/10.1111/j.1474-919X.2006.00510.x, 2006.

Gorelick, N., Hancher, M., Dixon, M., Ilyushchenko, S., Thau, D., and Moore, R.: Google Earth Engine: Planetary-scale geospatial analysis for everyone, Remote Sensing of Environment, 202, 18–27, https://doi.org/10.1016/j.rse.2017.06.031, big Remotely Sensed Data: tools,
470   applications and experiences, 2017.

Gusatu, L. F., Yamu, C., Zuidema, C., and Faaij, A.: A spatial analysis of the potentials for offshore wind farm locations in the North Sea region: Challenges and opportunities, ISPRS International Journal of Geo-Information, 9, 96, https://doi.org/10.3390/ijgi9020096, 2020.

Gușatu, L., Menegon, S., Depellegrin, D., Zuidema, C., Faaij, A., and Yamu, C.: Spatial and temporal analysis of cumulative environmental effects of offshore wind farms in the North Sea basin, Scientific Reports, 11, https://doi.org/10.1038/s41598-021-89537-1, 2021.

475   He, K., Zhang, X., Ren, S., and Sun, J.: Deep Residual Learning for Image Recognition, in: 2016 IEEE Conference on Computer Vision and Pattern Recognition (CVPR), pp. 770–778, https://doi.org/10.1109/CVPR.2016.90, 2016.

Henderson, A. R., Morgan, C., Smith, B., Sørensen, H. C., Barthelmie, R. J., and Boesmans, B.: Offshore Wind Energy in Europe— A Review of the State-of-the-Art, Wind Energy, 6, 35–52, https://doi.org/10.1002/we.82, 2003.

Hoeser, T. and Kuenzer, C.: Object Detection and Image Segmentation with Deep Learning on Earth Observation Data: A Review-Part I:
480   Evolution and Recent Trends, Remote Sensing, 12, https://doi.org/10.3390/rs12101667, 2020.

Hoeser, T. and Kuenzer, C.: SyntEO: Synthetic dataset generation for earth observation and deep learning – Demonstrated for offshore wind farm detection, ISPRS Journal of Photogrammetry and Remote Sensing, 189, 163–184, https://doi.org/10.1016/j.isprsjprs.2022.04.029, 2022a.

Hoeser, T. and Kuenzer, C.: DeepOWT: A global offshore wind turbine data set, https://doi.org/10.5281/zenodo.5933967, 2022b.

485   Hoeser, T., Bachofer, F., and Kuenzer, C.: Object Detection and Image Segmentation with Deep Learning on Earth Observation Data: A Review—Part II: Applications, Remote Sensing, 12, https://doi.org/10.3390/rs12183053, 2020.

Johnson, A. F., Dawson, C. L., Conners, M. G., Locke, C. C., and Maxwell, S. M.: Offshore renewables need an experimental mindset, Science, 376, 361–361, https://doi.org/10.1126/science.abo7924, 2022.

Kang, M., Ji, K., Leng, X., and Lin, Z.: Contextual Region-Based Convolutional Neural Network with Multilayer Fusion for SAR Ship
490   Detection, Remote Sensing, 9, https://doi.org/10.3390/rs9080860, 2017.

Krizhevsky, A., Sutskever, I., and Hinton, G. E.: ImageNet Classification with Deep Convolutional Neural Networks, pp. 1097–1105, http://papers.nips.cc/paper/4824-imagenet-classification-with-deep-convolutional-neural-networks.pdf, 2012.

Krizhevsky, A., Sutskever, I., and Hinton, G. E.: ImageNet Classification with Deep Convolutional Neural Networks, Communications of the ACM, 60, 84–90, https://doi.org/10.1145/3065386, 2017.

495   LeCun, Y., Bengio, Y., and Hinton, G.: Deep Learning, Nature, 521, 436–444, https://doi.org/10.1038/nature14539, 2015.

Loshchilov, I. and Hutter, F.: SGDR: Stochastic Gradient Descent with Warm Restarts, 2017.

Ma, L., Liu, Y., Zhang, X., Ye, Y., Yin, G., and Johnson, B. A.: Deep learning in remote sensing applications: A meta-analysis and review, ISPRS Journal of Photogrammetry and Remote Sensing, 152, 166 – 177, https://doi.org/10.1016/j.isprsjprs.2019.04.015, 2019.

Mullissa, A. G., Persello, C., and Tolpekin, V.: Fully Convolutional Networks for Multi-Temporal SAR Image Classi-
500   fication, in: IGARSS 2018 - 2018 IEEE International Geoscience and Remote Sensing Symposium, pp. 6635–6638, https://doi.org/10.1109/IGARSS.2018.8518780, 2018.

Opitz, J. and Burst, S.: Macro F1 and Macro F1, 2021.

Padilla, R., Passos, W. L., Dias, T. L. B., Netto, S. L., and da Silva, E. A. B.: A Comparative Analysis of Object Detection Metrics with a Companion Open-Source Toolkit, Electronics, 10, https://doi.org/10.3390/electronics10030279, 2021.

505 Reichstein, M., Camps-Valls, G., Stevens, B., Jung, M., Denzler, J., Carvalhais, N., and Prabhat: Deep learning and process understanding for data-driven Earth system science, Nature, 566, 195–204, 2019.

Ren, S., He, K., Girshick, R. B., and Sun, J.: Faster R-CNN: Towards Real-Time Object Detection with Region Proposal Networks, IEEE Transactions on Pattern Analysis and Machine Intelligence, 39, 1137–1149, 2015.

Rodrigues, S., Restrepo, C., Kontos, E., Teixeira Pinto, R., and Bauer, P.: Trends of offshore wind projects, Renewable and Sustainable
510 Energy Reviews, 49, 1114–1135, https://doi.org/10.1016/j.rser.2015.04.092, 2015.

Slavik, K., Lemmen, C., Zhang, W., Kerimoglu, O., Klingbeil, K., and Wirtz, K. W.: The large-scale impact of offshore wind farm structures on pelagic primary productivity in the southern North Sea, Hydrobiologia, 845, 35–53, https://doi.org/10.1007/s10750-018-3653-5, 2019.

Torres, R., Snoeij, P., Geudtner, D., Bibby, D., Davidson, M., Attema, E., Potin, P., Rommen, B., Floury, N., Brown, M., Traver, I. N., Deghaye, P., Duesmann, B., Rosich, B., Miranda, N., Bruno, C., L'Abbate, M., Croci, R., Pietropaolo, A., Huchler, M., and Rostan, F.:
515 GMES Sentinel-1 mission, Remote Sensing of Environment, 120, 9–24, https://doi.org/10.1016/j.rse.2011.05.028, the Sentinel Missions - New Opportunities for Science, 2012.

Virtanen, E., Lappalainen, J., Nurmi, M., Viitasalo, M., Tikanmäki, M., Heinonen, J., Atlaskin, E., Kallasvuo, M., Tikkanen, H., and Moilanen, A.: Balancing profitability of energy production, societal impacts and biodiversity in offshore wind farm design, Renewable and Sustainable Energy Reviews, 158, 112 087, https://doi.org/10.1016/j.rser.2022.112087, 2022.

520 Virtanen, P., Gommers, R., Oliphant, T. E., Haberland, M., Reddy, T., Cournapeau, D., Burovski, E., Peterson, P., Weckesser, W., Bright, J., van der Walt, S. J., Brett, M., Wilson, J., Millman, K. J., Mayorov, N., Nelson, A. R. J., Jones, E., Kern, R., Larson, E., Carey, C. J., Polat, İ., Feng, Y., Moore, E. W., VanderPlas, J., Laxalde, D., Perktold, J., Cimrman, R., Henriksen, I., Quintero, E. A., Harris, C. R., Archibald, A. M., Ribeiro, A. H., Pedregosa, F., van Mulbregt, P., and SciPy 1.0 Contributors: SciPy 1.0: Fundamental Algorithms for Scientific Computing in Python, Nature Methods, 17, 261–272, https://doi.org/10.1038/s41592-019-0686-2, 2020.

525 Wever, L., Krause, G., and Buck, B. H.: Lessons from stakeholder dialogues on marine aquaculture in offshore wind farms: Perceived potentials, constraints and research gaps, Marine Policy, 51, 251–259, https://doi.org/10.1016/j.marpol.2014.08.015, 2015.

Wilson, J. C. and Elliott, M.: The habitat-creation potential of offshore wind farms, Wind Energy, 12, 203–212, https://doi.org/10.1002/we.324, 2009.

Wong, B. A., Thomas, C., and Halpin, P.: Automating offshore infrastructure extractions using synthetic aperture radar and Google Earth
530 Engine, Remote Sensing of Environment, 233, 111 412, https://doi.org/10.1016/j.rse.2019.111412, 2019.

Xu, W., Liu, Y., Wu, W., Dong, Y., Lu, W., Liu, Y., Zhao, B., Li, H., and Yang, R.: Proliferation of offshore wind farms in the North Sea and surrounding waters revealed by satellite image time series, Renewable and Sustainable Energy Reviews, 133, 110 167, https://doi.org/10.1016/j.rser.2020.110167, 2020.

Zhang, J., Wang, Q., and Su, F.: Automatic extraction of offshore platforms in single SAR images based on a dual-step-modified model,
535 Sensors, 19, 231, 2019.

Zhang, T., Tian, B., Sengupta, D., Zhang, L., and Si, Y.: Global offshore wind turbine dataset, Scientific Data, 8, https://doi.org/10.1038/s41597-021-00982-z, 2021.

Zhu, X. X., Tuia, D., Mou, L., Xia, G., Zhang, L., Xu, F., and Fraundorfer, F.: Deep Learning in Remote Sensing: A Comprehensive Review and List of Resources, IEEE Geoscience and Remote Sensing Magazine, 5, 8–36, 2017.

540   Zhu, X. X., Montazeri, S., Ali, M., Hua, Y., Wang, Y., Mou, L., Shi, Y., Xu, F., and Bamler, R.: Deep Learning Meets SAR: Concepts, models, pitfalls, and perspectives, IEEE Geoscience and Remote Sensing Magazine, 9, 143–172, https://doi.org/10.1109/MGRS.2020.3046356, 2021.